Laser Thomson Scattering Measurements Indicate Non-Isothermal Magnetic Field Lines in Magnetically-Shielded Hall Effect Thrusters

Jean Luis Suazo Betancourt,[1] Naia Butler-Craig,[1] Julian Lopez-Uricoechea,[1] Adam M. Steinberg,[1] and Mitchell L. R. Walker[1]
School of Aerospace Engineering, Georgia Institute of Technology, Atlanta, GA 30318

(*Electronic mail: jlsb3@gatech.edu)

(Dated: 22 October 2024)

Expected high electron mobility and low resistivity along magnetic field lines – as compared to across magnetic field lines – have led to the assumption, or the reproduction through a solution to the electron energy equation, that magnetic field lines are isothermal in typical plasma simulations for Hall effect thrusters (HET). However, the inaccessibility of the near-field plasma region and perturbative nature of electrostatic probes have prevented validation of these assumptions in HETs. This manuscript presents non-intrusive measurements of the electron number density and electron temperature along two distinct magnetic field lines in the near-field discharge of a magnetically shielded HET operating at 150 V and 40 A on krypton based on incoherent laser Thomson scattering. The resulting electron temperature and density profiles indicate that the magnetic field lines are not isothermal or isopotential, with percent changes exceeding 100% of the channel-centerline electron temperature along each magnetic field line. This observation brings into question the current state of electron models in simulations and what physics are included, or neglected, to produce isothermal magnetic field lines in certain regions.

Keywords: Thomson scattering, electron velocity distribution functions, Hall effect thrusters, Bayesian inference

I. INTRODUCTION

Hall effect thrusters (HETs) are cross E×B field electrostatic devices that create thrust through the acceleration of ions produced by neutral propellant ionization with magnetized electrons from a hollow cathode electron source[1–4]. HETs are conventionally annular in shape with a single discharge channel, although non-conventional architectures have been the subject of several studies[5–7], and are reviewed in[8]. Modern HETs can be unshielded (US) or magnetically shielded (MS)[9,10].The main difference between US and MS thrusters lies in their magnetic field topology and channel wall chamfering.

A critical aspect of the operation of a HET is the electric field that accelerates ions out of the discharge channel to generate thrust. However, in addition to accelerating the bulk of ions out of the channel, potential structures stand up in the HET discharge channel that accelerate ions toward the insulating walls of the channel, causing channel erosion[11]. Early models predicted a potential structure along magnetic field lines that adhered to the Boltzmann relation, Equation 2 in Reference 12. This is a result of expected high electron mobility along the magnetic field lines, as compared with restricted mobility across them, leading to the assumption that magnetic field lines are isothermal[4,13]. Electrons are expected to be mobile when their resistance to movement and heat transport is low. This is quantified through a resistivity term in the generalized Ohms law[14].When this is the case, the field-line-parallel resistive terms in the vector form of Ohms law, deriving from the electron momentum equation, can be ignored[15]. Similarly, the field-line-parallel heat conduction term can be ignored in the electron energy equation[15]. If the field lines are indeed non-isothermal, this has implications for state-of-the-art HET plasma simulations. That is because these simulations recover isothermal magnetic field lines without this assumption, implying two things. First, that some physics are included or missing to arrive at these isothermal magnetic field lines. Second, that the potential gradients exist along magnetic field lines that lead the potential distribution to be non-Boltzmannian.

Studies of the potential structures in HETs have continued since their inception. The potential structure in a US HET was investigated at constant discharge voltage and varying current to study the location of the acceleration region. The acceleration region is the quasineutral region in the thruster discharge with a strong axial electric field[16]. This study showed the sensitivity of the beginning of the acceleration region to discharge condition[17]. Studies on the effect of segmented electrodes placed along the outer radius of the ceramic channel showed a significant influence on the acceleration and ionization regions due to changes in the potential structure of the thruster[18]. A 2D hydrodynamic model and a high-speed emissive probe were used to measure and explain the change in potential structure due to the segmented electrodes. However, these investigations were conducted with probes that perturbed the plasma and, thus, bring into question the validity of the measurements in this region[19,20].

Channel erosion is the life-limiting factor for US HETs. The erosion is the result of ion bombardment of the ceramic wall. The ions are accelerated into the wall by large sheath potential drops due to the high near-wall electron

temperature.These approximately radial field lines in US thrusters are not expected to be equipotential due to the high electron temperature and instead are broadly understood to follow potential distribution along the field line described by the Boltzmann relation[21]. The equipotentialized 'grazing' field lines in MS HETs keep near-wall electron temperatures low and the potential along the magnetic field line high, near the anode potential[9,10]. This directs the electric field away from the discharge channel wall and minimizes the sheath potential drop and, therefore, almost effectively eliminates erosion via ion bombardment. The 'grazing' field lines achieve this by extending deep into the channel where the electron temperature is low and enforcing equipotentialization, minimizing the sheath potential drops to the wall[21]

HETs leveraging more complex magnetic field topologies, like those present in MS HETs, bring into question the validity of the Boltzmann relationship for the potential along the magnetic field lines in the near-field discharge of MS HETs given the isothermality that goes into its construction. In particular, gradients in electron temperature may occur along the magnetic field lines that invalidate the isothermal approximation. Although MS does not assume that magnetic field lines are isopotential, isothermal magnetic field lines have been recovered self-consistently through simulation without explicitly assuming that the lines are isothermal, indicating that the mobility and resistivity assumptions in the electron models implicitly lead to this result[9,22].

Radial and axial magnetic field line gradients and gradients in the temperature distribution can lead to a potential structure along magnetic field lines that differs greatly from the Boltzmann relationship. Models that explicitly include temperature gradients, generalizing the Boltzmann relation, were developed and experimentally verified[23]. However, the role of deviation from thermalized magnetic field lines in complex magnetic field topologies, like those present in MS HETs, has not received extensive study.

The recent extension of MS HET operation to high and ultra-high current densities motivates the investigation of the validity of the isothermal magnetic field line model in the near field discharge of a high current density magnetically shielded HET[24–26]. The expected increased collisionality at current densities higher than the design point may increase transport across the field lines and decrease transport along them, which may make it less likely that the field lines are isothermal.

Given that the assumptions leading to the self-consistent reproduction of isothermal field lines in simulations or the assumption that the field lines are isothermal directly involve the electron properties, minimally invasive electron temperature and density measurements are required to investigate the limitations of the isothermal assumption and related models. Incoherent Laser Thomson scattering (LTS) provides a diagnostic that can be applied in the harsh near-plume plasma environment and provides direct measurements of electron thermal properties that are minimally invasive. Recently, LTS was used to study axial variation in electron properties and electron Mach number in hollow cathodes, heat flux and electron diffusion, and epirical closures for momentum and energy transport in the plume of a high power HET[27–29]. These measurements solidify the state-of-the-art in EP-relevant LTS diagnostics, demonstrating large-vacuum test facility LTS implementations for measurements in operating HET test articles.

The objective of this work is to make minimally invasive measurements of the electron temperature and density profiles along two distinct magnetic field lines in the near-field discharge of a MS HET to determine whether the magnetic field lines are isothermal.

This paper is structured as follows. Section II briefly describes the experimental setup of the LTS diagnostic, the test article, and discharge condition. It then briefly describes scattering theory, off-centerline stray light collection, and signal inversion procedures. Then, Section III presents and discusses the electron temperature and density profiles along two distinct magnetic field lines. Finally, conclusions and impact of the measurements are presented in Section IV.

II. EXPERIMENTAL SETUP AND ANALYSIS OF SCATTERING SIGNALS

A. Vacuum Test Facility

This experiment was conducted in the 4.9 m diameter and 9.2 m long stainless-steel Vacuum Test Facility 2 (VTF-2) at the Georgia Tech High Power Electric Propulsion Laboratory (HPEPL). The operation of VTF-2 is described in Kieckhafer and Walker[30]. Accurate knowledge of the chamber pressure during pump-down is important for calibration of the LTS measurements via laser Raman scattering. The instrumentation for measuring the facility pressure from atmospheric to high vacuum as well as the pressure correction methods are described in Suazo Betancourt *et al.*[28,31,32].

Mass flow was provided by two MKS GE40A mass flow controllers mounted externally to the facility. The mass flow controllers were calibrated in the test section of VTF-2 using a DryCal 800-10 volumetric flow rate meter system.

B. Thruster Discharge and Relative Motion

The test article in this experiment was the H9[33], shown in Figure 1, a 9-kW class MS HET referred to henceforth as "the thruster". The thruster is designed to operate with an internal and coaxial 60 A class lanthanum hexaboride (LaB_6) hollow cathode, whose design heritage stems from the HERMeS and H6 HETs hollow cathodes[34]. The H9 cathode is henceforth referred to as "the cathode". The operational envelopes of the H9 at

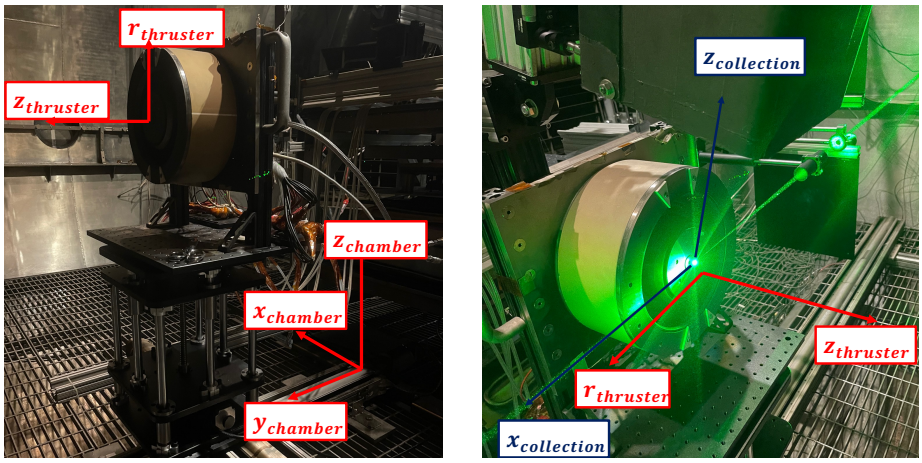

FIG. 1: Annotated picture of the HET and interrogation laser beam with all of the relevant basis vectors.

standard to ultra-high current densities are described in Refs.[24,33,35,36] and Refs[25,26], respectively.

The thruster coordinates used in this work (z, r, θ) have their origin at the thruster centerline and discharge channel exit plane, and are normalized by the thruster outer radius r_o. The vacuum chamber and light collection coordinates are as indicated in Figure 1. As described in Suazo Betancourt *et al.*[28], the LTS provides a point-wise measurement of the electron properties at a fixed location in space that is set by the intersection of the laser beam focus and the image of the fiber bundle through the inner-chamber collection optics.

The focused beam had an estimated 100 µm beam diameter, and the fiber bundle is 1:1 imaged on to the beam plane, with each of the seven fibers on the linear faces having a diameter of 200 µm. In order to spatially resolve the electron properties in the near-field thruster plume, the thruster was mounted on motion stages that allowed for three-axis movement relative to the laser beam, with a maximum positional uncertainty of 150 µm. The interrogation points were spaced by at least 1 mm axially and 2 mm radially, exceeding the approximately 1.4 mm×100 µm interrogation volume size in either direction.

Vibrations from the chamber and other equipment did not play a major role in positional uncertainty; however, the compression of the chamber relative to the external portions of the optical system impacted the system alignment. Optical realignment of the system was performed to mitigate thermal drift of the inner-chamber optics between every measurement point by aligning the laser beam through fixed targets inside of the chamber and by micrometer-level movement of the fiber inside of the chamber on electric motion stages. The system was deemed optimal when the signal at the cathode centerline matched the signal before the point was taken across the experiment. Before driving to each location, the motion stages were zeroed with respect to stoppers on the stages in order to ensure the absolute position with respect to the edges of the motion stages was respected. Suazo Betancourt *et al.*[28,31] provides more details this procedure.

The discharge condition for this experiment was taken to be 6 kW at a discharge voltage of 150 V and a discharge current of 40 A on krypton, well within the high current density regime described in Su *et al.*[25]. Signal-to-noise ratio issues at lower current density and the desire to expose the acceleration region motivated the high current density condition[16,32]. The coil current ratio and the absolute value of the coil currents did not vary between the "nominal" 6 kW condition and the high current density 6 kW condition. The thruster discharge circuit was floating for all experiments, with the cathode being electrically isolated from the thruster body. The supplies and instrumentation for driving the thruster and measuring the discharge telemetry are described in Suazo Betancourt *et al.*[32].

The magnetic field topology is expected to be the same as the originally quantified magnetic field topology across all H9 thrusters when the inner and outer coil current ratio is held constant[37]. In general, the field strength can vary with different operating conditions and propellant, as is noted in [35]. In general, the field strength is tuned to optimize for thruster stability by varying the absolute inner coil current value while holding constant the coil current ratio[35]. With this guidance, the optimal thruster stability field strength during our experiment could be compared to the work in Su *et al.*[35] to ensure that our value was reasonable. On krypton, the value of the field strength is expected to be 87.5% of that on xenon at the normal current density 6-kW condition. Our stability-

optimized field strength based on the absolute value of the inner coil current was the same as the normal current density condition. Additionally, measurement of the magnetic field strength at $z/r_o = .013$ along the channel centerline at our optimal inner coil current value indicated a difference of less than 1% with respect to the expected value at that location. Therefore, the magnetic field topology, which is dictated by the current ratio, and the maximum field strength relative to the nominal condition on xenon, which is indicated by the point-measured maximum magnetic field strength, are consistent with expectations and previous measurements. Additionally, simulations and measurements shared by collaborators at JPL showed that the magnetic field topology simulations and measurements differed by no more than 2% at the inner discharge channel walls, and were almost perfectly aligned in the near field plume region outside of the discharge channel[37]. Hence, the magnetic field topology at these conditions is expected to be consistent with previous measurements.

C. Interrogation, Collection, and Detection Optical Systems

The LTS collection and detection systems are thoroughly described in Suazo Betancourt *et al.*[28,32] with the latter providing details of the system as used in this work. We summarize the major components of the system below. The overall optical layout is shown in Figure 2.

An injection-seeded, frequency-doubled Amplitude DLS Powerlite 9010 Nd:YAG laser (9 mm diameter, pulse duration between 5 and 8 ns, 1 J/pulse at 532 nm) was used to stimulate the Thomson scattering, as well as Raman scattering used for absolute number density calibration. The laser beam was steered, externally to the vacuum chamber, along three legs that positioned the laser beam, oriented the polarization correctly relative to the scattering collection optical axis, focused the beam, and controlled the incident laser energy into the facility.

The light collection and detection system was designed to maximize the collection solid angle, provide a spatial resolution of less than 2 mm×2 mm, and facilitate realignment of the collection and interrogation optical axes when misalignment occurred due to facility shifts. Two FG200LEA- FBUNDLE custom fiber bundles were used in the collection system. The collection lenses and glass window protecting them were the same as those in the previous implementation. The collection optics were placed in a box to protect them from the plasma environment in the vacuum chamber, which was expected to be harsher than the previous stand-alone cathode experiments[28].

The angle of the collection axis with respect to the face of the face was approximately 17°. This allowed the collection volume to be positioned less than 1 mm from the thruster exit plane without the thruster hardware blocking the solid angle subtended by the collection optics. Note that the collection angle and direction of the scattering wave vector determine the component of the electron properties that are measured; in the current configuration, this component is not aligned with the thruster basis vectors. All reported electron temperatures are along the scattering wave vector. All data was taken at the 3 o'clock radial slice when facing the thruster. The temperature component is 17° forward (out of plane) with respect to the face of the thruster and 45° clockwise. Figure 3 shows the incident wave vector, scattering collection wave vector and its projection in the thruster plane, and the resulting projection of the scattering wave vector. Note that the electron temperature in HETs is known to be anisotropic[38]. Measurements taken by Lopez-Uricoechea *et al.*[16] show that in the current setup, the reported electron temperature is approximately the average of the azimuthal and radial electron temperatures. The literature suggests that the electron temperature in the component tangential to the magnetic field lines are constant[15]. Probing tangential to the magnetic field line will require varying the scattering wave vector. Although we are not probing with a scattering wave vector tangential to the magnetic field line, our measurements provide first insights into the electron properties along the magnetic field lines.

The spectrograph in this work was comprised of a Princeton Instruments ISOPLANE-320A spectrometer and PM4-1024i-HB-FG-18-P46 PIMAX4 ICCD camera. The spectrometer was operated with a motorized slit, slit shutter, and a 500-nm optimized 1200 l/mm grating. A four-lens relay system was used to capture all of the light from the fiber, relay it without clipping, and focus it into the spectrometer. The optical focal lengths were selected using ray-matrix optics in order to respect the Helmholtz optical invariant. The system used two 25 mm aperture volume Bragg grating notch filters from OptiGrate, recovering most of the collection power that was lost in previous work due to clipping on 15 mm aperture filters[28]. Note that these filters have become ubiquitous in EP LTS applications since the work by Vincent et al[39]. A Berkeley Nucleonics BNC-577-8C model delay generator was used as the master clock for the synchronization of timing events in the system.

D. Theory and Analysis of Scattering Signals

Laser rotational Raman scattering (LRS) is necessary in order to calibrate the absolute electron number density measurements in an LTS experiment. LRS is the inelastic scattering of incident radiation from polyatomic molecules as the result of a net exchange of energy from the incident radiation and the internal energy modes of the molecule[40,41]. The quantities of interest (QoI) in our calibration measurements ($\mathbf{x}^{\mathrm{R}}$) and so-called nuisance parameters (θ^{R}) that influence the scattered power but are not of primary interest to the measurement are

$$\mathbf{x}^{\mathrm{R}} = [\eta, \lambda_{\mathrm{i}}]^{\top}\,,\ \boldsymbol{\theta}^{\mathrm{R}} = [T_{\mathrm{g}}, \tau, p_{\mathrm{g}}]\,, \tag{1}$$

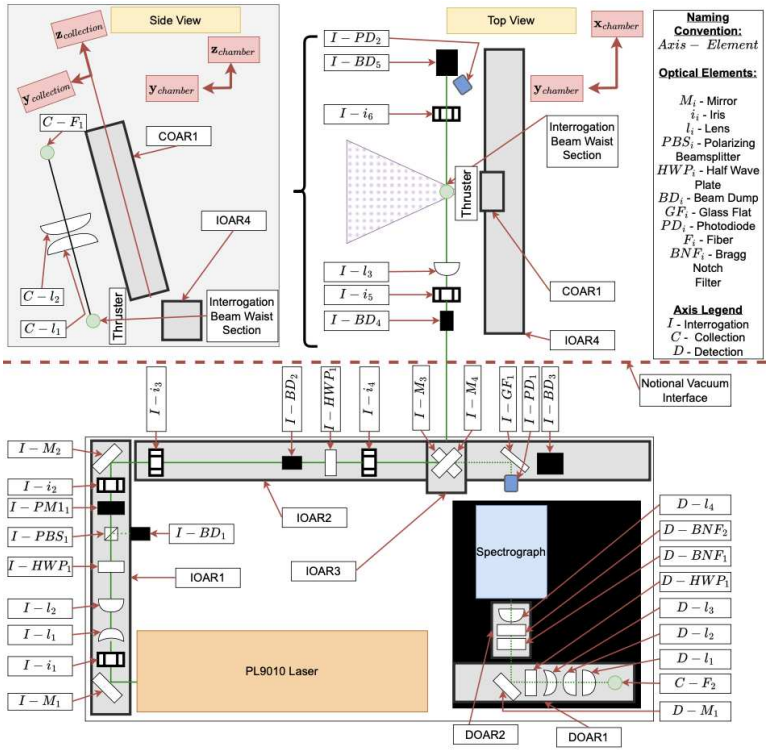

FIG. 2: Master optical diagram for the interrogation, collection, and detection systems. The vacuum interface is represented as the red dashed line. This figure was reproduced from Suazo Betancourt et al, Journal of Applied Physics 135 (2024)[28], with the permission of AIP Publishing.

where η, λ_i, T_g, τ, and p_g are the system efficiency calibration constant, incident laser wavelength, neutral gas temperature, full-width half maximum of the spectral redistribution function, and neutral gas pressure, respectively. The governing equations describing the relationship between the LRS scattering spectrum and parameters ($P_\lambda^R\left(\mathbf{x}^R, \boldsymbol{\theta}^R\right)$) are given in Suazo Betancourt *et al.*[28,42]

In all LRS cases, data were collected from air at a single local barometric-pressure-corrected value of 5 Torr. Multiple laser pulses were accumulated onto a single exposure of the ICCD camera, with the number of pulses set by camera saturation, to minimize read noise. On-chip binning was used in the direction perpendicular to the wavelength axis to minimize read noise and improve SNR. Binning along the wavelength-calibrated axis was not used to maintain spectral resolution. An invertible LRS spectrum was obtained from the measurements after subtraction of a background spectrum with the laser off.

LTS is the elastic electromagnetic scattering of incident radiation from unbounded charged particles and can be coherent or incoherent. Van de Sande[43] and Vincent[44] discuss the parameters determining whether an experimental setup and plasma conditions meet the conditions for coherent Thomson scattering; incoherent LTS is relevant here. For LTS, the wavelengths of the scattered radiation are consistent with the Doppler-shifted motion of the individual electrons along the scattering wave vector $\mathbf{k}$[44,45]. This is directly linked to the relative velocity of the observer and the scattering electron along the scattering wave vector, viz. $\mathbf{k} \equiv \mathbf{k}_i - \mathbf{k}_s$, with $\mathbf{k}_i$ being the incident propagation wave vector and $\mathbf{k}_s$ being the wave vector along the direction from the scattering volume to the observer.

The total scattered power is redistributed over the spectral band dictated by the electron velocity distribution function (EVDF) along the scattering wave vector. For a plasma whose electron population is in ther-

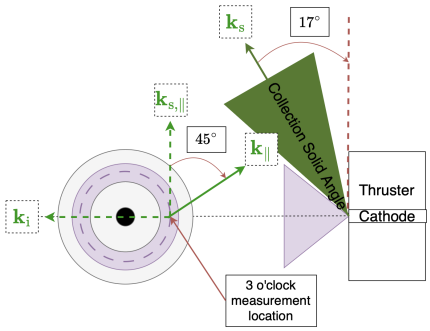

FIG. 3: Left and front diagram of the thruster and the scattering configuration. $\mathbf{k}_i$ is the incident wave vector, $\mathbf{k}_s$ is the scattering collection wave vector, and $\mathbf{k}$ is the scattering wave vector with $\parallel$ denoting the projections/components in the plane parallel to the thruster face.

mal equilibrium, the spectral distribution function $S_k(\lambda)$ corresponds to a Maxwellian EVDF that can be related to the equilibrium electron temperature T_e; the classical electron temperature is the full descriptor for the shape of the distribution in such plasmas[44,46]. The governing Maxwellian model equations ($P_\lambda^T\left(\mathbf{x}^T, \boldsymbol{\theta}^T\right)$) fit to the LTS signals can be found in Suazo Betancourt *et al.*[42], and are parameterized by the QoI and nuisance parameter vectors,

$$\mathbf{x}^T = [T_e, n_e, v_d]^\top, \quad \boldsymbol{\theta}^T = [\eta, \lambda_i]^\top, \tag{2}$$

with T_e, n_e, v_d being the electron temperature, electron density, and the magnitude of the bulk drift velocity along the scattering wave vector. Note that the scattering wave vector is not guaranteed to be parallel to any particular hardware feature of an experimental configuration at all measurement locations given the construction of the collection system. There are certain system configurations where the scattering wave vector can be completely aligned with desired thruster axes at specific measurement locations, like the radial and azimuthal directions in Reference 38. In the current configuration, the scattering wave vector is not completely parallel to either the azimuthal or axial axes regardless of measurement location given the 17 degree inclination of the collection axis with respect to the $\boldsymbol{\theta}$-$\mathbf{z}$ plane of the thruster. At the 3 o'clock measurement location used in this work, the normalized scattering wave vector is described by Equation 3[16].

$$\frac{\mathbf{k}}{|\mathbf{k}|} = \sin(17°)\hat{\mathbf{z}} + \cos(17°)\cos(45°)\left(\hat{\mathbf{r}} - \hat{\boldsymbol{\theta}}\right) \tag{3}$$

For details on deriving the reconciliation between the scattering wave vector and the thruster axis vectors, see references 16,38. Further, Bayesian model selection applied to the data in this thruster support the Maxwellian plasma assumption[32].

In general, four spectra are required in order to produce an invertible LTS spectrum. The desired LTS spectrum, a spectrum to remove plasma emission, a spectrum to remove stray light from sources other than the plasma and elastic laser scattering, and a spectrum to remove several sources of noise and the detector background bias. These signals are typically collected with the laser on and the plasma on, laser off and the plasma on, laser on and the plasma off, and finally, laser off and the plasma off, respectively. All background corrections other than the one for stray light were addressed in Suazo Betancourt *et al.*[28]

The main source of stray light in the current experiments is laser induced fluorescence, generated when the measurement volume is close to fluorescent material in the thruster hardware[44]. Hence, a stray light correction image was taken at every measurement location (with the plasma off) using the same laser power and imaging settings as the LTS. Similar to Vincent[44], the magnitude of the fluorescence spectra increased linearly with wavelength from about 539 nm to the highest wavelength measured. This linear fit was used to correct the measured LTS spectra for fluorescent stray light at every measurement location. Further details of the correction are described in Lopez-Uricoechea *et al.*[16]

All measured signals – both LRS and LTS spectra – were inverted to find the QoI (and nuisance parameters) using a Bayesian framework[42]. The advantage of the Bayesian framework compared to more common least-squared analysis lies in its rigorous propagation and quantification of uncertainty through the entire signal inversion process, from the LRS through to LTS. Furthermore, in the LTS inversion, the Bayesian framework provides a rigorous assessment on the reliability of the plasma model underlying the signal inversion via the Bayes' factor. The result of the LRS or LTS signal inversion process is a posterior probability density function (PDF) $\mathbb{P}^i(\mathbf{x}^i, \theta^i|\mathbf{b})$ following Bayes' equation,

$$\mathbb{P}^i(\mathbf{x}^i, \theta^i|\mathbf{b}) = \frac{\mathbb{P}^i(\mathbf{b}|\mathbf{x}^i, \theta^i)\mathbb{P}^i(\mathbf{x}^i, \theta^i)}{\mathbb{P}(\mathbf{b})}. \tag{4}$$

Here, $\mathbb{P}^i(\mathbf{b}|\mathbf{x}^i, \theta^i)$, $\mathbb{P}^i(\mathbf{x}^i, \theta^i)$, and $\mathbb{P}(\mathbf{b})$ are the likelihood, prior, and evidence PDFs, $\mathbf{b}$ is the data for a given measurement, and i indicates whether the PDFs and parameters pertain to a LRS measurement ($i = \mathrm{R}$) or LTS measurement (inverted using a Maxwellian plasma model, $i = \mathrm{T}$), etc. The posterior is a comprehensive description of one's knowledge of the QoI following a measurement, carrying all the measured and prior information about the QoI and nuisance parameters.

In this work, the likelihood distributions, parameters used to construct the prior probability distribution functions, etc. are the same as in Suazo Betancourt *et al.*[42] The posterior estimates from the LRS inference are used to construct the priors for the nuisance parameters for

the LTS inference. The PDFs were sampled using a Markov-chain Monte Carlo method. For the sake of computational efficiency, the length of the Markov chains was limited to 50,000 samples from the posterior using a Metropolis-Hastings algorithm. These samples were used to determine the maximum a posteriori (MAP) estimates of the QoI and quantify the uncertainty. In the results that follow, individual data points are the MAP values of the QoI and the error bars represent plus and minus twice the standard deviation for each parameter.

III. RESULTS AND DISCUSSION

A. Normalized Axial Measurement Locations and Thruster Discharge Telemetry

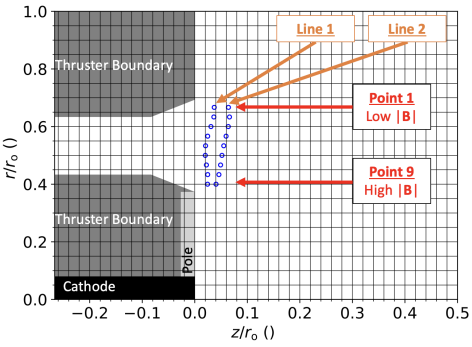

FIG. 4: Normalized magnetic field line measurement locations in blue. The field lines are numbered one to two from left to right, and the magnetic field line points are numbered one to nine from top to bottom on each respective field line. The thruster boundaries are represented in grey, the front pole cover in light grey, and the cathode keeper body in black.

The measurement locations for this experiment are presented in Fig. 4. Field lines 1 and 2 intersect the discharge channel centerline with normalized axial positions of $z/r_o = .02$, and $z/r_o = .055$, respectively. The average facility operational pressure (P_O), anode mass flow rate ($\dot{m}_A$), cathode mass flow rate ($\dot{m}_C$), discharge voltage (V_D), discharge current (I_D), and the peak frequencies for the discharge circuit (f_{V_D}, f_{I_D}), respectively, are tabulated in Table I. The measurement location point number along each field line ($\hat{s}_j$) increases from the outer discharge channel edge ($\hat{s}_j = 1$) to inner discharge channel edge ($\hat{s}_j = 9$); the discharge channel centerline point is $\hat{s}_j = 5$ along each field line. The first field line, $B_i = 1$, is closer to the discharge channel exit plane than the second field line. Throughout the results, we will refer to the measurement locations by point number and field line number.

B. Electron Properties Along Magnetic Field Lines

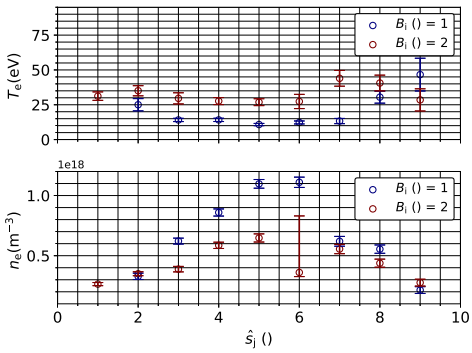

FIG. 5: Electron temperature and density profiles along the outlined magnetic field lines. The field lines (B_i) are numbered from left to right, and the points along each field line $\hat{s}_j$ are numbered from top to bottom along each field line in 4.

The electron temperature and density profiles along the first and second magnetic field lines are presented in Figure 5. Two representative spectra, one along line 1 at $\hat{s}_j = 5$ (discharge channel centerline), and the second along line two at $\hat{s}_j = 9$ (inner channel edge), are presented in Figure 6. The electron temperature (in eV) is observed to exceed 20% of the discharge voltage (in V). This observation is similar to that of recent works by Suazo Betancourt *et al.*[32] and Roberts *et al.*[29,47] where LTS measurements produce electron temperatures that are twice the scaling traditionally expected via electrostatic probes, see Haas *et al.*[48–50]. However, it is prudent to discuss several artificial sources of broadening and their possible effect on the inverted spectra presented here. As stated in Suazo Betancourt *et al.*[28,42] , the instrument function full width half max (FWHM), which represents the spectral redistribution on incoming light due to the spectrograph, was solved for in the LRS inversion inversion but was not explicitly included in the LTS inversion, as in other similar work by Vincent *et al.*[38]. This was due to the fact that the FWHM of the instrument function is less than an order of magnitude smaller than that of our observed LTS spectra, with FWHMs of less than 1 nm with the 500 µm spectrometer slit width and grating pitch of 1200 l/mm used as opposed to the approximately 10 nm FWHMs present in the LTS spectra. Including this effect would serve to decrease the FWHM of the LTS spectra by less than 1-2 eV, and lead

TABLE I: Hall effect thruster discharge telemetry for the measurements taken along the two distinct magnetic field lines. For the traces collected corresponding to each of these parameters, a mean and standard deviation was associated with respect to the peak-to-peak oscillations. The values reported below are the ensemble average across all traces collected.

P_{O} (Torr-Kr)	$\dot{m}_{\mathrm{A}}$ (mg/s)	$\dot{m}_{\mathrm{C}}$ (mg/s)	V_{D} (V)	I_{D} (V)	$f_{V_{\mathrm{D}}}$ (kHz)	$f_{I_{\mathrm{D}}}$ (kHz)
7.05×10.0^{-6} $\pm1.8\%$	23.5±1.0%	1.78±1.0%	150.8±4.2%	40.2±16.4%	6.5±1.0%	6.4±1.0%

to a lower temperature estimates. With respect to this source of broadening, our temperature estimates may be high by no more than 1-2 eV. This instrument broadening effect is discussed in [27]. Works by Dale *et al.*[51] and Konopliv *et al.* [52] suggest that the electron temperature and density fluctuations are significantly out of phase, and we therefore expect that an ensemble average over 3000-6000 frames to not artificially broaden our spectra. The main source of artificial broadening can be attributed to the case in which the number density detection limit is being approached, where the signal can be misinterpreted as being artificially wide if it is not sufficiently high above the noise floor. However, in the lowest peak signal to mean noise cases during this experiment, the SNR exceeded 2, giving us confidence that our measurements were not artificially broadened. The electron temperature is lower for the magnetic field line closer to the discharge channel exit B_1. Along each field line, higher temperatures occurred towards the channel edges ($\hat{s}_j = 1, 9$) as compared to the discharge channel centerline ($\hat{s}_j = 5$). The electron density is higher for the field line closer to the discharge channel exit. Note that the $\hat{s}_6$ point along the B_2 field line had an artificially low density due to optical misalignment during the acquisition of the point, even though the system was realigned between acquiring all points. This was confirmed by noting the maximum signal strength during the beginning of the alignment before the next point. The choice was made not to repeat the acquisition of this point due to time constraints and to highlight this alignment challenge as a future area of improvement. A more robust method for maintaining alignment will be deployed in the next iteration of the measurement system.

The electron pressure profile, calculated via $P_{\mathrm{e}} = n_{\mathrm{e}} k_{\mathrm{b}} T_{\mathrm{e}}$, along the magnetic field lines is presented in Fig. 7. The electron pressure shows a variation of over 50 % compared to the centerline electron pressure value ($\hat{s}_j = 5$) along both magnetic field lines. The variation in electron pressure indicates that the magnetic field lines, at least at this high current density operating condition, are not isopotential. The recent work by Roberts *et al.*[47] also conclude that the temperature along magnetic field lines is non-isothermal. However, they observe qualitatively different radial variations in the electron properties, with our temperature increasing as we get further from the channel centerline while theirs decreases. This can be attributed to the movement of the acceleration zone. In their case, the acceleration zone is speculated to shift axially into the channel with increasing voltage, with a modest peak suggesting the acceleration region is located just outside of the channel at their lowest voltage, which is twice our voltage in this case. This is consistent with the work in Chaplin *et al.*[53] indicating downstream movement of the acceleration zone with decreasing voltage. The work by Suazo Betancourt *et al.*[32] shows the axial variation of the electron temperature along the discharge channel centerline, with the peak temperature located at $z/r_{\mathrm{o}} = .1$, which is further downstream than the furthest magnetic field line. We therefore expect that the field line measurements in our experiment, as opposed to work by Roberts *et al.*[47], were probed ahead of the acceleration zone. That, coupled with the less accentuated rise in temperature along the second field line, which is further from the exit plane, suggests that ahead of the acceleration zone, the temperature can be expected to increase radially away from the discharge channel centerline and then transition to the behavior observed in Roberts *et al.*[47]. However, a similar parametric study into the high current density domain would be required to confirm this. Additionally, as previously stated, lower discharge voltage shifts the expected location of the acceleration of the region axially downstream. With an approximately constant acceleration region length, there will be a reduction in the strength of the electric field because of a reduction in discharge voltage. The lower electric field is expected to reduce the E×B velocity of the electrons. And, a shift of the acceleration region downstream would move it into a region of lower magnetic field strength. Both of these effects are expected to reduce the Ohmic heating and lead to a lower electron temperature, which is what we observed given that our peak centerline electron temperature is less than half of what was observed at the 300 V 15 A condition in[29].

From the electron momentum equation, in the case of a steady-state electrostatic plasma that is collisionless with negligible electron momentum and an isotropic thermalized closure for the pressure tensor, the relationship between the electrostatic potential ϕ and electron pressure P_{e} is given by

$$\nabla\phi = \frac{1}{q_{\mathrm{e}} n_{\mathrm{e}}} \nabla P_{\mathrm{e}}, \tag{5}$$

where q_{e} is the electron charge. In the case where the

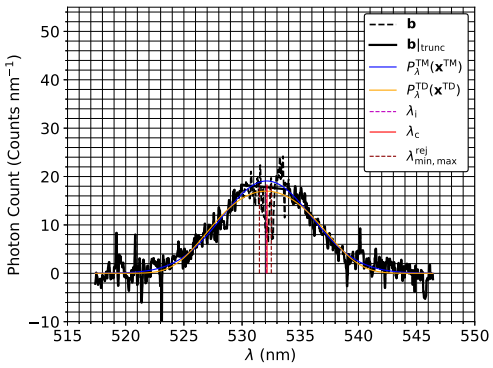

(a)

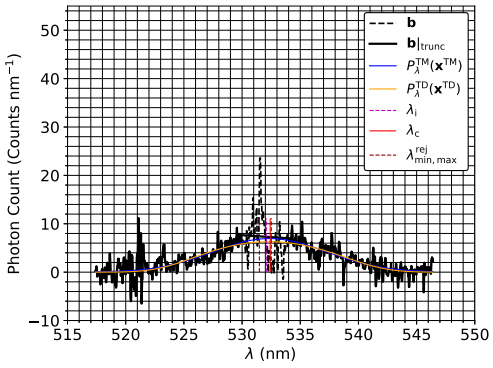

(b)

FIG. 6: Raw and model spectra for the laser Thomson scattering inversions at two representative points, with (a) and (b) being along line 1 at $\hat{s}_j = 5$ (discharge channel centerline), and the second along line 2 at $\hat{s}_j = 9$ (inner channel edge). Figures (a) and (b) both show the raw and truncated ($\mathbf{b}$ and $\mathbf{b}|_{\text{trunc}}$) model spectra for Maxwellian ($P_\lambda^{\text{TM}}\left(\mathbf{x}^{\text{TM}}\right)$) and Druyvesteyn ($P_\lambda^{\text{TD}}\left(\mathbf{x}^{\text{TD}}\right)$) spectral distribution function, evaluated at the most probable value of the input parameters. Please see References 42 and 28 for more details.

temperature along the magnetic field line is constant, the isothermal magnetic field lines recover the thermalized potential relationship, also known as the Boltzmann relation.[12].

However, Figure. 5 shows significant variation of T_e along the magnetic field lines, with percent changes with respect to the mean centerline value exceeding 100%. Indeed, as far back as the work of Morozov[13], the assumption of high mobility along the magnetic field lines

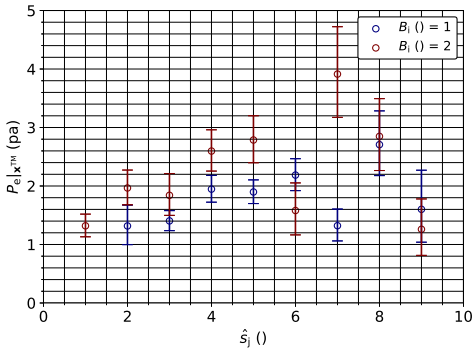

FIG. 7: Electron pressure along each magnetic field line.

has been used to set the along-field electron temperature gradient to zero, thus recovering a thermalized potential. However, at the given discharge condition, the magnetic field lines are not strictly isothermal and can therefore not adhere to the thermalized potential model, in contrast with the traditional electron model assumptions[3,4,12].

IV. CONCLUSIONS

The work provides the first-ever non-intrusive measurements of electron temperature and electron number density along two distinct magnetic field lines in a HET. These measurements indicate that the temperature along the magnetic field lines is not constant, suggesting that the isothermal assumption in the discharge region of magnetically shielded, high-current HETs may need to be revisited in order to accurately account for the variation in the electron temperature along the field lines.These measurements were conducted in a configuration whose scattering wave vector was largely perpendicular to the plane of the magnetic field lines being probed. Given that HET plasma electron temperatures are expected to be anisotropic[38], a future in-plane scattering configuration would be beneficial.

Our results are limited to the 150 V, 40 A operating condition. Previous work on the applicability of this model suggested that curvature affects the applicability of the model[54]. The region traversed by the field line, as well as the curvature of the field line, are found to play a role in the deviation from isothermalized magnetic field lines, given that the electron temperature and density are found to vary radially even at constant axial location, and vice versa, as seen in Reference[32]. However, it is possible to maintain a constant potential in accordance with the general assumptions of the isothermal model before the assumption of isothermality is in place. A calcula-

tion of the electrostatic potential gradient in magnetic field line coordinates in one dimension indicates a non-zero gradient in the electrostatic potential. This indicates that, in the probed architecture, the magnetic field lines cannot be considered strictly isothermal or isopotential. Additionally, the lines are observed to deviate from the isothermal and isopotential models closer to areas of increased magnetic field strength towards the acceleration region and the channel edge.

The results motivate the need to make similar measurements at several operating conditions to understand the effect of discharge conditions on the isothermal assumption. Additionally, the measurements motivate revisiting simulations that reproduce isothermal magnetic field lines to understand why they are observed not to be isothermal. Given that the mobility of electrons across and along magnetic field lines constitutes one of the conceptually foundational operating principles for HETs, this may point to requiring more targeted magnetic field line experiments to bridge the gaps in understanding electron mobility with respect to magnetic field lines. Within the larger world of magnetized plasmas, these minimally invasive measurements will allow for a more accurate understanding of fundamental phenomena that plague all magnetized plasmas, from HETs to Tokamaks. This includes mobility across and along magnetic field lines.

V. ACKNOWLGEMENTS

The authors would like to thank Professor Samuel J. Grauer for his contributions to the Bayesian framework used in the processing of the data in this manuscript.

[1]D. M. Goebel and I. Katz, *Fundamentals of Electric Propulsion: Ion and Hall Thrusters* (Wiley, 2008).
[2]R. G. Jahn, "Physics of Electric Propulsion," (Dover Publications, 2006) pp. 1–50.
[3]V. V. Zhurin, H. R. Kaufman, and R. S. Robinson, "Physics of closed drift thrusters," Plasma sources science & technology **8**, R1–R20 (1999).
[4]V. Kim, "Main Physical Features and Processes Determining the Performance of Stationary Plasma Thrusters," Journal of Propulsion and Power **14**, 736–743 (1998).
[5]B. Pote, V. Hruby, and R. Tedrake, "Performance of a multi-kilowatt non-circular discharge Hall thruster," in *36th AIAA/ASME/SAE/ASEE Joint Propulsion Conference and Exhibit* (2006) p. 3249.
[6]S. E. Cusson, M. P. Georgin, H. C. Dragnea, E. T. Dale, V. Dhaliwal, I. D. Boyd, and A. D. Gallimore, "On channel interactions in nested Hall thrusters," Journal of Applied Physics **123**, 133303 (2018).
[7]B. Beal, A. Gallimore, and W. Hargus, "The Effects of Cathode Configuration on Hall Thruster Cluster Plume Properties," in *41st AIAA/ASME/SAE/ASEE Joint Propulsion Conference & Exhibit* (American Institute of Aeronautics and Astronautics, Reston, Virigina, 2005).
[8]Chhavi C. and M. L. R. Walker, "Review of Non-conventional Hall Effect Thrusters," Journal of Electric Propulsion (2024).
[9]I. G. Mikellides, I. Katz, R. R. Hofer, and D. M. Goebel, "Magnetic shielding of a laboratory Hall thruster. I. Theory and validation," Journal of Applied Physics **115** (2014), 10.1063/1.4862313.
[10]R. R. Hofer, D. M. Goebel, I. G. Mikellides, and I. Katz, "Magnetic shielding of a laboratory Hall thruster. II. Experiments," Journal of Applied Physics **115** (2014), 10.1063/1.4862314.
[11]J. P. Boeuf, "Tutorial: Physics and modeling of Hall thrusters," Journal of Applied Physics **121** (2017), 10.1063/1.4972269.
[12]I. G. Mikellides, R. R. Hofer, I. Katz, and D. M. Goebel, "Magnetic shielding of Hall thrusters at high discharge voltages," Journal of Applied Physics **116** (2014), 10.1063/1.4892160.
[13]A. I. Morozov and V. V. Savelyev, "Fundamentals of Stationary Plasma Thruster Theory," in *Reviews of Plasma Physics* (Springer, 2000) pp. 203–391.
[14]I. G. Mikellides and A. L. Ortega, "Challenges in the development and verification of first-principles models in Hall-effect thruster simulations that are based on anomalous resistivity and generalized Ohm's law," Plasma Sources Science and Technology **28**, 14003 (2019).
[15]I. G. Mikellides and I. Katz, "Numerical simulations of Hall-effect plasma accelerators on a magnetic-field-aligned mesh," Physical Review E - Statistical, Nonlinear, and Soft Matter Physics **86** (2012), 10.1103/PhysRevE.86.046703.
[16]J. Lopez-Uricoechea, J. L. Suazo Betancourt, N. Butler-Craig, and M. L. R. Walker, "Spatially resolved Thomson scattering measurements of electron properties across the acceleration region of a high-power magnetically shielded Hall effect thruster," Journal of Applied Physics **136** (2024), 10.1063/5.0213928.
[17]J. M. Haas and A. D. Gallimore, "Internal plasma potential profiles in a laboratory-model Hall thruster," Physics of Plasmas **8** (2001), 10.1063/1.1338535.
[18]Y. Raitses, M. Keidar, D. Staack, and N. J. Fisch, "Effects of segmented electrode in Hall current plasma thrusters," Journal of Applied Physics **92** (2002), 10.1063/1.1510556.
[19]B. Jorns, D. M. Goebel, and R. R. Hofer, "Plasma Perturbations in High-Speed Probing of Hall Thruster Discharge Chambers: Quantification and Mitigation," in *51st AIAA/SAE/ASEE Joint Propulsion Conference* (American Institute of Aeronautics and Astronautics, Reston, Virginia, 2015).
[20]L. Grimaud, A. Pétin, J. Vaudolon, and S. Mazouffre, "Perturbations induced by electrostatic probe in the discharge of Hall thrusters," Review of Scientific Instruments **87** (2016), 10.1063/1.4945563.
[21]I. G. Mikellides, I. Katz, R. R. Hofer, and D. M. Goebel, "Magnetic shielding of walls from the unmagnetized ion beam in a Hall thruster," Applied Physics Letters **102** (2013), 10.1063/1.4776192.
[22]I. G. Mikellides, D. M. Goebel, B. A. Jorns, J. E. Polk, and P. Guerrero, "Numerical simulations of the partially ionized gas in a 100-A LaB6 hollow cathode," IEEE Transactions on Plasma Science **43** (2015), 10.1109/TPS.2014.2320876.
[23]M. Keidar, A. D. Gallimore, Y. Raitses, and I. D. Boyd, "On the potential distribution in hall thrusters," Applied Physics Letters **85** (2004), 10.1063/1.1797555.
[24]L. L. Su, A. R. Vazsonyi, and B. Jorns, "Performance of a 9-kW Magnetically-Shielded Hall Thruster with Krypton," in *AIAA Propulsion and Energy 2020 Forum* (American Institute of Aeronautics and Astronautics, Reston, Virginia, 2020).
[25]L. L. Su and B. Jorns, "Performance at High Current Densities of a Magnetically-Shielded Hall Thruster," in *AIAA Propulsion and Energy 2021 Forum* (American Institute of Aeronautics and Astronautics, Reston, Virginia, 2021).
[26]L. L. Su, P. J. Roberts, T. Gill, W. Hurley, T. A. Marks, C. L. Sercel, M. Allen, C. B. Whittaker, M. Byrne, Z. Brown, E. Viges, and B. Jorns, "Operation and Performance of a Magnetically Shielded Hall Thruster at Ultrahigh Current Densities on Xenon and Krypton," in *AIAA Scitech 2023 Forum* (American Institute of Aeronautics and Astronautics, Reston, Virginia, 2023).
[27]P. J. Roberts and B. Jorns, "Characterization of Electron Mach Number in a Hollow Cathode with Thomson Scattering," in *AIAA Scitech 2023 Forum* (American Institute of Aeronautics and Astronautics, Reston, Virginia, 2023) pp. 1–1.

[28]J. L. Suazo Betancourt, N. Butler-Craig, J. Lopez-Uricoechea, J. Bak, D. Lee, A. M. Steinberg, and M. L. R. Walker, "Thomson scattering measurements in the krypton plume of a lanthanum hexaboride hollow cathode in a large vacuum test facility," Journal of Applied Physics **135** (2024), 10.1063/5.0180251.
[29]P. J. Roberts and B. A. Jorns, "Laser measurement of anomalous electron diffusion in a crossed-field plasma," Physical Review Letters (2024).
[30]A. W. Kieckhafer and M. L. R. Walker, "Recirculating Liquid Nitrogen System for Operation of Cryogenic Pumps," in *32nd International Electric Propulsion Conference* (Electric Rocket Propulsion Society, Wiesbaden, Germany, 2011).
[31]J. L. Suazo Betancourt, *Laser Thomson Scattering Measurements of the Plasma Structure in the Front Pole Region of a Magnetically-shielded Hall Effect Thruster*, Ph.D. thesis, Georgia Institute of Technology, Atlanta (2024).
[32]J. L. Suazo Betancourt, J. Lopez-Uricoechea, N. Butler-Craig, A. M. Steinberg, and M. L. R. Walker, "Bayesian-inverted laser Thomson scattering measurements indicate electrostatic erosion pathways in magnetically-shielded Hall effect thrusters," Journal of Applied Physics **136** (2024), 10.1063/5.0221547.
[33]R. R. Hofer, S. E. Cusson, R. B. Lobbia, and A. D. Gallimore, "The H9 Magnetically Shielded Hall Thruster," in *35th International Electric Propulsion Conference, Atlanta, GA* (Electric Rocket Propulsion Society, 2017).
[34]S. J. Hall, R. E. Florenz, A. Gallimore, H. Kamhawi, D. L. Brown, J. E. Polk, D. M. Goebel, and R. R. Hofer, "Implementation and Initial Validation of a 100-kW Class Nested-channel Hall Thruster," in *50th AIAA/ASME/SAE/ASEE Joint Propulsion Conference* (American Institute of Aeronautics and Astronautics, Reston, Virginia, 2014).
[35]L. L. Su and B. A. Jorns, "Performance comparison of a 9-kW magnetically shielded Hall thruster operating on xenon and krypton," Journal of Applied Physics **130** (2021), 10.1063/5.0066849.
[36]S. E. Cusson, R. R. Hofer, R. B. Lobbia, B. A. Jorns, and A. D. Gallimore, "Performance of the H9 Magnetically Shielded Hall Thrusters," in *35th International Electric Propulsion Conference, Atlanta, GA* (Electric Rocket Propulsion Society, 2017).
[37]J. Simmonds, R. R. Hofer, and M. L. R. Walker, "Personal communication of the H9v2 200G Magnetic Field Map between High-Power Electric Propulsion Laboratory Director and Electric Propulsion Group at NASA Jet Propulsion Laboratory," (2022).
[38]B. Vincent, S. Tsikata, and S. Mazouffre, "Incoherent Thomson scattering measurements of electron properties in a conventional and magnetically-shielded Hall thruster," Plasma Sources Science and Technology **29**, 35015 (2020).
[39]B. Vincent, S. Tsikata, S. Mazouffre, T. Minea, and J. Fils, "A compact new incoherent Thomson scattering diagnostic for low-temperature plasma studies," Plasma Sources Science and Technology **27**, 55002 (2018).
[40]D. A. Long, "Classical Theory of Rayleigh and Raman Scattering," in *The Raman Effect: A Unified Treatment of the Theory of Raman Scattering by Molecules* (Wiley, 2002) pp. 31–48.
[41]N. John and S. George, "Raman spectroscopy," in *Spectroscopic Methods for Nanomaterials Characterization* (Elsevier, 2017) pp. 95–127.
[42]J. L. Suazo Betancourt, S. J. Grauer, J. Bak, A. M. Steinberg, and M. L. R. Walker, "Bayesian plasma model selection for Thomson scattering," Review of Scientific Instruments **95** (2024), 10.1063/5.0158749.
[43]M. J. van de Sande, *Laser scattering on low-temperature plasmas: High resolution and stray light rejection*, Ph.D. thesis, Eindhoven Technical University (2004).
[44]B. Vincent, *Incoherent Thomson scattering investigations in Hall thruster, planar magnetron and ECR ion source plasmas*, Ph.D. thesis, ICARE - Institut de Combustion, Aérothermique, Réactivité et Environnement, Orleans (2019).
[45]D. H. Froula, S. H. Glenzer, N. C. Luhmann, and J. Sheffield, "Scattered Power Spectrum," in *Plasma Scattering of Electromagnetic Radiation* (Elsevier, 2011) pp. 31–44.
[46]W. G. Vincenti, C. H. Kruger, and T. Teichmann, " Introduction to Physical Gas Dynamics ," (Krieger Pub Co, 1975).
[47]P. J. Roberts, M. G. Allen, D. G. Brick, and B. A. Jorns, "Empirical Closures for Momentum and Energy Transport in Hall Thrusters based on Thomson Scattering Measurements," in *38th International Electric Propulsion Conference* (Electric Rocket Society, Toulouse, 2024).
[48]J. M. Haas and A. D. Gallimore, "nternal plasma potential profiles in a laboratory-model Hall thruster," Physics of Plasmas **8**, 652–660 (2001).
[49]J. M. Haas, *Low-perturbation Interrogation of the Internal and Near-field Plasma Structure of a Hall Thruster Using a High Speed Probe Positioning System*, Ph.D. thesis, University of Michigan, Ann Arbor (2001).
[50]R. R. Hofer, *Development and Characterization of High-Efficiency, High-Specific Impulse Xenon Hall Thrusters*, Ph.D. thesis, The University of Michigan, Ann Arbor (2004).
[51]E. T. Dale and B. A. Jorns, "Non-invasive time-resolved measurements of anomalous collision frequency in a Hall thruster," Physics of Plasmas **26** (2019), 10.1063/1.5077008.
[52]M. F. Konopliv, R. E. Wirz, and L. K. Johnson, "Ion-Neutral Density and Electron Temperature Phasing in the Hall Thruster Breathing Mode," in *Ion-Neutral Density and Electron Temperature Phasing in the Hall Thruster Breathing Mode* (Electric Rocket Propulsion Society, Toulouse, 2024).
[53]V. H. Chaplin, B. A. Jorns, A. Lopez Ortega, I. G. Mikellides, R. W. Conversano, R. B. Lobbia, and R. R. Hofer, "Laser-induced fluorescence measurements of acceleration zone scaling in the 12.5 kW HERMeS Hall thruster," Journal of Applied Physics **124** (2018), 10.1063/1.5040388.
[54]J. Geng, L. Brieda, L. Rose, and M. Keidar, "On applicability of the "thermalized potential" solver in simulations of the plasma flow in Hall thrusters," Journal of Applied Physics **114** (2013), 10.1063/1.4821018.